Identifying recharge under subtle ephemeral features in flat-lying semi-arid region using a combined geophysical approach

Brady A. Flinchum[1], Eddie Banks[2], Michael Hatch[2,3], Okke Batelaan[2], Luk Peeters[1], Sylvain Pasquet[4]

[1]Commonwealth Scientific Industrial Research Organization (CSIRO), Deep Earth Imaging Future Science Platform & Land
5   and Water, Urrbrae, 5064, Australia
[2] National Centre for Groundwater Research and Training, College of Science and Engineering, Flinders University, Adelaide,
5001, Australia
[3] Department of Geosciences, School of Physics, University of Adelaide, Adelaide, Australia
[4] Université de Paris, Institut de physique du globe de Paris, CNRS, F-75005 Paris, France.

10   *Correspondence to*: Brady A. Flinchum (brady.flinchum@csiro.au)

Abstract. Identifying and quantifying recharge processes linked to ephemeral surface water features is challenging due to their
episodic nature. We use a unique combination of well-established near-surface geophysical methods to provide evidence of a
surface and groundwater connection under a small ephemeral recharge feature in a flat, semi-arid region near Adelaide,
Australia. We use a seismic survey to obtain P-wave velocity through travel-time tomography and S-wave velocity through
15   the multichannel analysis of surface waves. The ratios between P-wave and S-wave velocities allow us to infer the position of
the water table. A separate survey was used to obtain electrical conductivity measurements from time-domain electromagnetics
and water contents were acquired by downhole nuclear magnetic resonance. The combined geophysical observations provide
evidence to support a groundwater mound underneath a subtle ephemeral feature. Our results suggest that recharge is localized
and that small-scale ephemeral features play an important role in groundwater recharge. Furthermore, we show that a combined
20   geophysical approach can provide a unique perspective that helps shape the hydrogeological conceptualization of a semi-arid
region.

1 Introduction

Understanding groundwater recharge mechanisms and surface water-groundwater connectivity is crucial for
sustainable groundwater management (Banks et al., 2011; Brunner et al., 2009). In semi-arid areas, recharge has been shown
25   to occur in focused regions beneath perennial streams and lakes, and ephemeral streams and ponds (Cuthbert et al., 2016;
Scanlon et al., 2002, 2006). However, identifying localized regions of groundwater recharge remains challenging.

Many aquifers in semi-arid areas receive a significant portion of their recharge from adjacent mountain ranges
(Bresciani et al., 2018; Earman et al., 2006; Winograd et al., 1998). In this common scenario, recharge can occur via
groundwater flow from the mountain range directly into the aquifer—implying a significant lateral groundwater connection
30   with the adjacent mountain range (Batlle-Aguilar et al., 2017). Alternatively, precipitation from the mountain range flows out

and across the semi-arid basin as surface water and recharge the aquifer via river infiltration processes—implying a vertical connection between surface and groundwater (Bresciani et al., 2018; Brunner et al., 2009; Winter et al., 1998).

Groundwater recharge processes span a wide range of spatial and temporal scales making them difficult to quantify (Scanlon et al., 2002). Recharge rates are traditionally quantified using physical, tracer, or modelling techniques (Scanlon et
35 al., 2002). Physical techniques include carefully measuring fluxes and evapotranspiration along various reaches of a river or stream (Abdulrazzak, 1995; Lamontagne et al., 2014) or through stream hydrograph separation (Banks et al., 2009; Chapman, 1999; Cuthbert et al., 2016). Common tracer techniques include the use of stable isotopes of hydrogen and oxygen (Lamontagne et al., 2005; Taylor et al., 1992; Winograd et al., 1998), quantifying chemical signatures that have accumulated from past human activities (Cook et al., 1996), and measuring environmental tracers such as chloride (Allison et al., 1990;
40 Anderson et al., 2019; Crosbie et al., 2018) and Radon (Bertin and Bourg, 1994; Genereux and Hemond, 2010; Hoehn and Gunten, 1989). Lastly, numerical modelling is used to estimate recharge over global scales (Gleeson et al., 2012; Scanlon et al., 2006) and test existing hydrogeological conceptualizations (Xie et al., 2014).

Quantifying recharge processes in ephemeral ponds or streams is particularly difficult because flooding events are episodic (Shanafield and Cook, 2014). The infrequency and variable size of flooding events makes it difficult to monitor,
45 quantify, or even identify if groundwater recharge has occurred. Furthermore, infiltration is a different process than recharge. Groundwater recharge must be confirmed by a response in the water table, whereas water that has infiltrated might have been taken up by vegetation or lost to evaporation. Understanding how ephemeral features interact with groundwater remains a challenge. Larger ephemeral rivers flood frequently so equipment can be installed and be ready when an event occurs (Dahan et al., 2007, 2008). On the other hand, it is more difficult to capture recharge events of smaller ephemeral tributaries; as a
50 result, the recharge mechanisms of these features are less understood. These smaller scale features are common on Earth's surface. It has been shown that 69% of first-order streams and ~34% of larger fifth-order rivers below 60° latitude are ephemeral (Acuña et al., 2014; Raymond et al., 2013). Thus, even if small ephemeral features only provide small amounts of groundwater recharge during individual events, their large spatial distribution means that they could be important to recharge processes of a given region.

55 Small ephemeral features are an ideal size for near-surface geophysical surveys. A wide range of existing and standardized geophysical techniques have been used in hydrological studies (e.g. Robinson et al., 2008; Siemon et al., 2009; Parsekian et al., 2015). To highlight surface and groundwater connections, geophysical methodologies commonly rely on time-lapse measurements. This is because the infiltration of groundwater causes changes in geophysical properties on the order of days or months (i.e. the geology stays constant). Time-lapse electrical resistivity measurements have been used to observe and
60 monitor recharge pathways (Carey and Paige, 2016; Singha and Gorelick, 2005; Johnson et al., 2012; Valois et al., 2016; Thayer et al., 2018; Kotikian et al., 2019) and can highlight preferential flow paths. These methods are still handicapped by the fact that they still require the burial or setup of the geophysical equipment prior to a natural recharge (Kotikian et al., 2019; Thayer et al., 2018) or a man-made event (Carey and Paige, 2016; Claes et al., 2019). A geophysical approach that can be

deployed rapidly (that is without a time-lapse setup) to determine if an ephemeral drainage feature is acting as a groundwater

65   recharge feature over a flat landscape does not yet exist.

The aim of this study is to use a unique combination of well-established near-surface geophysical methods to provide evidence of a surface and groundwater connection of a small, shallow, and subtle ephemeral feature in a low-lying semi-arid landscape without time-lapse measurements. We used a single seismic survey to obtain P-wave velocity through seismic refraction tomography (SRT) (Sheehan et al., 2005; Zelt et al., 2013) and S-wave velocity through the multi-channel analysis

70   of surface waves (MASW) (Park et al., 1999; Pasquet and Bodet, 2017). A separate survey was used to obtain bulk electrical conductivity measurements from time-domain electromagnetics (TEM) (Parasnis, 1986; Reynolds, 2011; Telford and Telford, 1976). Water contents and T_2 relaxation times (time constant for the decay of transverse magnetization) were acquired using downhole nuclear magnetic resonance (NMR) (Walsh et al., 2013). We used this unique combination of standard geophysical measurements to show that small-scale ephemeral features likely contribute to the replenishment of groundwater in shallow

75   unconfined aquifers as localized recharge in low-lying semi-arid regions.

2 Site Description

The North Adelaide Plains (NAP) is located north of the city of Adelaide, Australia and is part of the St Vincent Basin, a geological basin underlying the area between the Yorke Peninsula and the Mount Lofty Ranges in South Australia (Figure 1). The St Vincent Basin is a north south trending basin that is characterized by low topographic relief between 0 and

80   200 m elevation above sea level (Smith et al., 2015). The NAP is bound by the Mount Lofty Ranges to the East and its northern boundary is marked by the Light River (Figure 1). Land-use in the NAP is predominantly dryland agriculture with mixed farming (sheep and rotational cropping of wheat, barley, and canola) (The Goyder Institute for Water Research, 2016). Potential evaporation is high and the average rainfall is low, averaging around 445 mm·yr^{-1}, with an average daily temperature of 21.6 °C (Bresciani et al., 2018). The combination of low rainfall and high evaporation rates in the NAP implies that the

85   source water in the aquifers is from the Mount Lofty Ranges where the average rainfall is 983 mm·yr^{-1} (Bresciani et al., 2018). Rainfall is winter-dominated (May to August), which suggests that recharge is also seasonal (Batlle-Aguilar et al., 2017; Bresciani et al., 2018).

Within the NAP there are three main hydrogeological sedimentary units that provide groundwater for the region (Department for Water, 2010; The Goyder Institute for Water Research, 2016). The first is a series of aquifers that occurs

90   within the overlying Quaternary rocks referred to as aquifers Q1-Q4. In the Quaternary aquifers, salinity ranges between 2000 and 13,000 mg·L^{-1} (Department for Water, 2010; The Goyder Institute for Water Research, 2016). Below the Quaternary aquifers is an unconfined aquifer comprised of limestones and sandstones, referred to as the T1 aquifer. The T1 aquifer shows a significant increase in salinity (from 500-1,000 mg.L^{-1} to 7000-14,000 mg.L^{-1}) moving north across the NAP (Department for Water, 2010; The Goyder Institute for Water Research, 2016). Underlying the T1 aquifer is a confined aquifer system, also

95   comprised of limestones and sandstones, referred to as the T2 aquifer. In the T2 aquifer there is an east-west trough, where

salinity increases from 500-1,000 mg·L^{-1} to 7000-14,000 mg·L^{-1} over 10 km from the centre of the trough (The Goyder Institute for Water Research, 2016). Both the T1 and T2 aquifers are used for irrigation, while the Q1-Q4 aquifers are typically used for stock and domestic purposes and only monitored because they present a risk of waterlogging and soil salinization (Department for Water, 2010). The work within this manuscript focuses on the surface and groundwater connections within

100 the Quaternary sediments.

The NAP is characterized by minimal topographic relief. LiDAR of the region shows that within this low relief landscape there are many small ephemeral surface drainage features (Figure 1). These subtle drainage features are visible in the hill-shaded LiDAR (Figure 1d) and indicates that surface water runoff is likely to flow towards these ephemeral drainage features and the larger streams after large precipitation events (Figure 1d). These ephemeral features are not monitored because

105 they fall below the resolution of the 30 m SRTM elevation data (Figure 1d).

Although there is consensus that the water that recharges the NAP aquifers comes from the Mount Lofty Ranges to the East, the flow paths along which this occurs is still debated. There are currently two competing conceptual models. The first argues that water flows from the Mount Lofty Ranges onto the NAP through ephemeral rivers and streams and recharges the underlying aquifers via vertical infiltration (Bresciani et al., 2018). In this model recharge is localized and occurs along the

110 main rivers and streams. This conceptual model is supported by lower groundwater chloride concentrations surrounding the Gawler River in both the Quaternary and Tertiary aquifers and the piezometric surfaces that show groundwater moving away from the rivers (losing river conditions) and into the underlying aquifers (Bresciani et al., 2018). In contrast, the second model argues that the aquifers of the NAP are recharged through a lateral groundwater connection with the rocks underlying the Mount Lofty Ranges (Batlle-Aguilar et al., 2017). This interpretation is supported by an increase in groundwater ages away

115 from the Mount Lofty Ranges and stable isotopes indicating some evaporation prior to infiltration (Batlle-Aguilar et al., 2017).

Our study site is located on a private farm, 44 km northwest of Adelaide and is between the Light and Gawler rivers (Figure 1). In May of 2018, 47 shallow holes were drilled across the northern region of the NAP with a small truck-mounted Rockmaster drill rig (Figure 1b). The holes were drilled to at least 6 m depth using a 40 mm diameter push core, producing a continuous core sample. Our study transect for the near surface geophysical surveys was located adjacent to one of these drill

120 hole sites where we had manual water level measurements, soil samples, and downhole NMR logs. The 235-m-long transect line was positioned so that it crossed a small ephemeral topographic feature. The drill hole occurs at 220 m along the transect (Figure 1c). Due to limited site access and in order to increase our chances of observing the water table with the geophysical data, we chose a site where the shallow water table was anticipated to be within 3-10 m depth below the ground surface.

3 Methods

125 To aid in geophysical interpretation and reduce ambiguities, it is important to "ground-truth" near-surface geophysical data with drilling results (Flinchum et al., 2018; Gottschalk et al., 2017; Orlando et al., 2016; West et al., 2019) or to corroborate them by other independent geophysical measurements. In this study, we combined hydrogeological observations with multiple

geophysical measurements to obtain different geophysical parameters, specifically: bulk electrical conductivity from TEM, P-wave velocity from SRT, S-wave velocity from MASW, and water contents from downhole NMR. In April 2018, the shallow drillhole was logged with a downhole NMR system (Vista Clara Dart) and the water level was measured by hand. Only a week after the seismic data were collected, a separate campaign was carried out to collect 26 TEM soundings along the same profile (Figure 1c). In the following manuscript, we use these geophysical methods to infer a surface water-groundwater connection without time-lapse measurements. In this section we briefly describe the theory behind the geophysical methods and how the measurements are influenced by various hydrological properties. Additional figures and details pertaining to the processing of the geophysical data set can be found in the supplementary material.

3.1 Topography Acquisition

At our study site, no LiDAR imagery was available. High resolution imagery of the small study area (~9 hectares) was thus acquired with a DJI Phantom 4 Pro unmanned aerial vehicle (UAV). The UAV flew a grid pattern over the study area at an elevation of 30 m above ground level and collected a photo dataset of 834 images. Georeferencing was undertaken using a Trimble R10 global positioning system (GPS) Real Time Kinematic (RTK) survey with 65 ground control points located within the study area and provided a georeferencing root mean square error (RMS) of 0.153 meters. The captured photos were processed using the photogrammetry Pix4D software package (Pix4Dmapper Pro version 3.2, 2017) to generate a high resolution (0.8 cm/pixel) digital surface model (DSM). As the study area was a fallow field at the time of the survey, the DSM was treated as a digital elevation model (DEM) as there was very little vegetation present. The generated DEM was re-sampled to a 0.5 m DEM (Figure 1) that was used to extract the elevation profile along the geophysical transect.

3.2 Seismic Refraction Tomography

Seismic refraction is an active source geophysical method that estimates seismic velocity. A seismic refraction survey provides a spatial distribution of P-wave velocity (energy propagating along the direction of travel). In a shallow seismic refraction survey, the time taken for the energy to travel from a source to each individual receiver, called a travel-time, is measured. The subsurface velocity structure controls the travel-times so they can be inverted to retrieve the subsurface P-wave velocity structure using a forward model and an inversion scheme (Sheehan et al., 2005; Zelt et al., 2013). P-wave velocity is controlled by the elastic properties of the material, porosity, and saturation (Berryman et al., 2002; Hashin and Shtrikman, 1963). If the pore space is filled with a fluid, in our case water (regardless of salinity), then the P-wave velocity is greater than if the pore space is not filled with fluid (Bachrach and Nur, 1998; Desper et al., 2015; Gregory, 1976; Nur and Simmons, 1969).

In this survey, we used 48 geophones spaced at 5 m, which produced a 235 m long profile. The source was a 40 kg accelerated weight, striking a 20 x 20 x 2 cm steel plate at every geophone. To increase the signal-to-noise, 8 shots were stacked at each of the 80 locations. The travel-times were picked manually (Figure S1 and S2) and inverted for P-wave velocity using the refraction module in the Python Geophysical Inversion and Modeling Library (pyGIMLi) (Rücker et al., 2017). The

160   forward model is based on the shortest path algorithm (Dijkstra, 1959; Moser, 1991; Moser et al., 1992). PyGIMLi utilizes a deterministic Gauss-Newton inversion scheme and incorporates a data weight matrix (Rücker et al., 2017). We populated the data weight matrix using reciprocal travel-times (Figure S2). To initialize the inversion, we used a gradient model that had a velocity of 0.4 km·s^{-1} at the surface and 2 km·s^{-1} at a depth of 40 m. To quantify uncertainty, we incorporated a bootstrapping algorithm on the travel-time picks (details in the supplementary material). The model fits are determined by a χ^2 misfit, which

165   incorporates our picking errors and a root mean square (RMS) error (details in supplementary material).

3.3 Multichannel Analysis of Surface Waves

At the Earth's surface, most of the elastic energy travels as surface waves. Surface waves are the largest amplitude events that are recorded in both active source seismic acquisition and earthquake records. Surface waves are caused by interactions of the body waves (P-waves and S-waves) and the boundary conditions that only exist at the surface (Stein and

170   Wysession, 1991). There are two types of surface waves: Love waves and Rayleigh waves (for a detailed review on surface waves, the reader is referred to Stein and Wysession, 1991; Lowrie, 2007). In this study we take advantage of the dispersive nature of Rayleigh waves, which means that different frequencies travel at different speeds (Park et al., 1999; Pasquet and Bodet, 2017; Xia et al., 1999, 2003). Furthermore, Rayleigh waves propagate at velocities mostly driven by the S-Wave velocity of the medium. The dispersion of Rayleigh waves can be measured by picking the phase velocity as a function of

175   frequency (Park et al., 1999; Xia et al., 2003). The phase velocity of lower frequencies (longer wavelengths) will be influenced by deeper S-wave velocity structures whereas higher frequencies will be influenced by shallower structures. These frequency dependent phase velocities can then be inverted for one-dimensional (1D) S-wave velocity models at low computational costs (Pasquet and Bodet, 2017).

In this study, we use the acquisition set up from the refraction survey to analyse the dispersion of surface wave energy.

180   This approach produces a pseudo two-dimensional (2D) section comprised of 41 1D S-wave velocity profiles, spaced every 5 m starting at 17.5 m from the start of the profile. To build the pseudo 2D profile we used the Surface Wave Inversion and Profiling (SWIP) package (Pasquet and Bodet, 2017). First, the seismic data is resorted and windowed to sample 1D vertical slices of the subsurface. Once windowed, the sorted seismic data are transformed into the frequency-phase velocity domain using a slant stack (Mokhtar et al., 1988). To increase the depth of investigation, similar dispersion curves from different shots

185   are stacked together (Neducza, 2007). Once the dispersion curves are constructed they are picked and an uncertainty associated with each pick is defined (O'Neil, 2003) (Figure S4). To construct our dispersion curves, we used 40 m windows (8 stations) and ensured a 5 m offset between the source and first channel to avoid near-source effects. The picks and corresponding uncertainty for each windowed dispersion curve are inverted using a Monte Carlo approach and the neighbourhood algorithm (Sambridge, 1999; Wathelet et al., 2004). We ran 15,000 inversions for each of our dispersion curves and averaged the 1000

190   best-fitting S-wave velocity models to build final 1D models (Figure S5) every 5 m (more details about processing can be found in the supplementary material). Finally, the individual 1D S-wave profiles are combined into a pseudo-2D section (Pasquet et al., 2015b, 2015a; Pasquet and Bodet, 2017).

3.4 Poisson's Ratio

Locating the water table of the unconfined aquifer over large spatial scales is challenging and is traditionally done by
195   drilling down to the water table and interpolating manual water level measurements between drillhole locations. Building a
detailed water table map requires many measurements and can be limited by logistical or financial constraints. Here, we can
exploit the fact that P-wave velocities increase when a material is saturated and the S-wave velocities remain relatively
unchanged (Bachrach and Nur, 1998; Desper et al., 2015; Gregory, 1976; Nur and Simmons, 1969).

Poisson's ratio is a unitless elastic property that describes how much a material will deform in the direction
200   perpendicular to an applied stress. Poisson's ratio can be calculated from P-wave and S-wave velocities (Eq. 1).

$$v = \frac{V_p^2 - 2V_s^2}{2(V_p^2 - V_s^2)}, \tag{1}$$

In Eq. 1, V_p is P-wave velocity, V_s is S-wave velocity and v is Poisson's ratio. Poisson's ratio for geologic materials
ranges from 0 to 0.5. Poisson's ratio increases as fluid saturation increases (Bachrach et al., 2000; Dvorkin and Nur, 1996; Nur
and Simmons, 1969; Salem, 2000). Furthermore, Poisson's ratio is an indicator for determining the difference between gas
205   and fluid saturated materials (Gregory, 1976; Pasquet et al., 2016) and has been shown to be useful to track pressure changes
(Prasad, 2002), map the water table depth (Bachrach et al., 2000; Pasquet et al., 2015b; Salem, 2000; Uyanık, 2011), and
differentiate gas and fluid in hydrothermal systems (Pasquet et al., 2016). To image the water table with Poisson's ratio, the
conceptual model of the geology must be simplified (i.e. no lateral changes) and requires that there are at least a few meters of
unsaturated sediments overlying the saturated region to generate a vertical contrast in the elastic; our study site satisfies both
210   these conditions.

3.5 Nuclear Magnetic Resonance

Nuclear magnetic resonance (NMR) capitalizes on the existence of a measurable magnetic moment produced by the
rotation of hydrogen protons contained in water molecules. At equilibrium, the direction of the magnetic moment points in the
direction of a background magnetic field. An NMR measurement emits an electromagnetic pulse at a specific frequency (called
215   Larmor frequency) in order to force protons out of equilibrium. When the excitation pulse ends, the protons return to
equilibrium in a process called relaxation. During relaxation, a measurable resonating magnetic moment that decays
exponentially can be measured (Bloch, 1946; Brownstein and Tarr, 1979; Torrey, 1956). The initial magnitude of the signal is
directly proportional to the number of protons excited, which in near-surface exploration come mostly from groundwater, and
the rate of decay (i.e. the relaxation time T_2) is related to the pore size. Thus, NMR has a unique ability to directly measure the
220   amount of groundwater within its measurement volume. For a thorough review of NMR theory, the reader is referred to
(Behroozmand et al., 2015) and textbooks dedicated to the theory of NMR (Coates et al., 1999; Dunn et al., 2002; Levitt,
2001).

The decay rate, described by T_2, is a function of two distinct processes: the bulk relaxation and the surface relaxation (Brownstein and Tarr, 1979; Cohen and Mendelson, 1982; Grunewald and Knight, 2012). The surface relaxation is controlled
225   by an intrinsic property called the surface relaxivity and the surface-to-pore volume ratio. Surface relaxivity describes a material's ability to intensify relaxation. The dependence on the surface-to-pore volume ratio is what relates the NMR decay to the pore scale properties. In general, materials with larger pores spaces have longer T_2 relaxation times (e.g. gravels) and materials with smaller pores have shorter T_2 (e.g. clays). When high quality data is acquired, such as with downhole systems, the T_2 relaxation times can be fit using multi-exponential decay curves. The distribution of decay times represents the properties
230   of all the pores within the excited volume. We acquired downhole NMR measurements at 0.25 m depth intervals down a 7.5 m drill hole using a Dart system (Vista Clara). The Dart quantifies water content and T_2 decay times in two cylindrical shells of varying radii (12.7 and 15.2 cm) within the drillhole.

3.6 Transient Electromagnetics (TEM)

The transient electromagnetic method utilizes a transmitting and receiving loop lying on the earth's surface. The TEM
235   method specifically uses a short-transmitted pulse duration and measures the decay amplitude of the vertical component of the electromagnetic field generated by secondary currents as a function of time. The magnitude and decay rate of the vertical electromagnetic field is related to the electrical conductivity of the subsurface beneath the loop. The penetration depth of the method depends on the underlying conductivity structure and the size of the transmitting loop and the amplitude of the transmitted signal. For a more thorough description of the TEM technique see Telford (1976), Parasnis (1986), or Reynolds
240   (2011).

We collected the TEM data using a Zonge Engineering NanoTEM system. The NanoTEM is a low-power, fast-sampling time-domain TEM system that was specifically designed to provide high resolution images of the near-surface (~50 metres depth). The NanoTEM data were collected using a 20 m x 20 m square transmitter loop with a 5 m x 5 m, single-turn receiving loop. The transmitter coil had an output current of 2 A and a turnoff of ~ 2 μs. The receiving loop sampled at 625
245   kHz, stacking 256 cycles at a repetition rate of 32 Hz. The stacks were averaged and then inspected to remove noisy data in the late times. The NanoTEM data were inverted using the Aarhusinv program, run using "smooth model" settings (Auken et al., 2006, 2015). The 1D inversion assumes laterally homogeneous layers. All NanoTEM soundings were inverted separately (i.e. there were no lateral constraints,) and placed next to one another and interpolated to generate pseudo 2D profiles of bulk electrical conductivity. The quality of the inversion is determined by a misfit value between the observed and modelled
250   voltages.

3.7 Drillhole Soil Sample Measurements

Soil samples were collected at 0.25 m intervals from the continuous core that was retrieved during the shallow drilling program. Each soil sample was placed into an air-tight plastic container to prevent moisture loss and preserved for later analysis in the laboratory for gravimetric water contents and soil pore water salinity. The gravimetric water content was determined as

255   the water loss between the wet and dry sample after three days in an oven at 40 degrees, using standard methodologies as described in Rayment and Higginson (1992). Salinity (i.e. electrical conductivity) of the pore water was measured using a 1:5 mass ratio by combining 20 g of soil and 100 g of ultra-pure water (Rayment and Lyons, 2011). The samples were agitated by rotating in a tumbler device for 48 hours, left to settle for one hour and then an electrical conductivity probe was used to measure the electrical conductivity of the supernatant. The soil water conductivity was determined using the 1:5 ratio dilution

260   factor. For the shallow drillhole, we have gravimetric water content and soil conductivity as a function of depth. To make comparisons with the NMR data, the gravimetric water content was converted into volumetric water content by multiplying an assumed soil density between 1.3-1.5 g·cm^{-3}. We also assumed the density of water equal to 1 g·cm^{-3}.

4 Results

4.1 Seismic Results

265   The P-wave velocity profile is characterized by two distinct features. The first feature is a laterally homogeneous layer defined by a consistent increase in velocity from about 0.3 km·s^{-1} to 1.5 km·s^{-1}. The bottom of the feature is defined by a velocity of ~1.5 km·s^{-1} and corresponds to the depth where the vertical velocity gradient weakens significantly (Figure 2b). This boundary, which is clearly identified in the travel-time picks (Figure S2), defines the bottom of an approximately 13-m-thick horizontal layer at around 0 m elevation (Figure 2). The second feature is more subtle and is associated with a change of

270   slope in the travel-time picks between 60 and 80 m (Figure S2a). Because of the high quality of the seismic data, the inversion was able to adjust this change in slope in the travel-time curves (Figure S2) which is reflected in the final model (Figure 2). This high velocity structure is subtle, but clearly shows up in the vertical gradient space (Figure 2b). At this location, both the vertical gradient and the velocities increase just below a depression existing at the surface (Figure 2).

Like the P-wave velocity profile, the S-wave profile is laterally continuous (Figure 3a). On average the S-wave

275   velocity increases from 0.2 km·s^{-1} at the surface to 0.4 km·s^{-1} in the deepest parts of the model. There is an abrupt increase in velocity around 0 m elevation (Figure 3), which is consistent with the large change in velocity observed in the P-wave velocity profile (Figure 2). There is one notable difference between the two profiles occurring between 60 and 80 m., approximately at the same location where we observed the subtle increase in P-wave velocities; unlike the P-wave velocities, the S-wave velocities are defined by a slight decrease in velocity (Figure 3) which was also a clear and observable feature in the picked

280   dispersion curves (Figure S4).

4.2 TEM Results

The 26 NanoTEM soundings show consistency between the soundings (Figure 4a). To ease comparisons to both the S-wave and P-wave profiles, the soundings (Figure 4a-b) were interpolated to a 2.5 x 0.5 m grid. In this grid the distance along the x-axis is relative to the start of the seismic profile (Figure 1). The interpolation was done using an adjustable tension

285   continuous curvature spline (Smith and Wessel, 1990). In the interpolated section (Figure 4b), the most resistive feature (<

200 mS·m^{-1}) occurs at the ground surface and extends to an elevation of 10 m above mean sea level (m a.m.s.l.) between 60 to 80 m along the profile. The resistive feature is well constrained by individual soundings (Figure 4a) and extends both laterally and at depth on both sides of the depression between 10 and 5 m a.m.s.l. and from 40 to160 m along the profile (Figure 4b).

4.3 NMR and Soil Sample Results

290   The downhole NMR results show that the volumetric water contents of the soil profile vary between 0 and 0.25 m^3/m^3, with a gradual increase with depth (Figure 5a). The maximum water content of 0.25 m^3/m^3 was measured between 6.75 and 7 m depth, consistent with the measured water level depth (6.8 m) (Figure 5a). The average amplitude of the noise in the water contents determined by NMR is ~0.05 m^3/m^3. Therefore, inverted water contents less than 0.05 m^3/m^3 are less reliable. Signals from the soundings can be found in the supplementary material (Figure S6). Above the water table, the NMR data showed a 295 rise in water contents above 0.05 m^3/m^3 between 1.75 and 3 m depth. The water within this region contains low T_2 relaxation times (< 0.01 s). A similar pattern in water content and T_2 decay times occurs between 4 and 6 m depth (Figure 5a and 5b). Around 6 m depth the T_2 distributions transition from shorter to longer (>0.01 s) relaxation times and the water contents also increase (Figure 5b). This gradual increase in the T^2 decay times and water content is likely to be the capillary fringe, where the remaining pore space fills from smallest to largest pores. At depths below the measured water level (6.8 m), the T_2 300 distributions normalize and have a value just over 0.01 s, which is consistent with clays. The gravimetric water content measured from the drill hole core samples had an average of 0.15 with a standard deviation of 0.02 and showed very little variation with depth (Figure 5c). The soil pore water conductivity also showed little variation with depth, having an average conductivity of 1123 µS·cm^{-1} with a standard deviation of 424 µS·cm^{-1} (Figure 5c). In contrast, the measured groundwater conductivity was 14750 µS·cm^{-1} (conductivity of sea water is ~50000 µS·cm^{-1}).

305 ## 5 Discussion

5.1 Geophysically Inferred Water Table Depth

     We use the P-wave profile generated by travel-time tomography (Figure 2a), the S-wave profile estimated through the inversion of surface waves (Figure 3), and Eq. 1 to create a Poisson's ratio profile (Figure 6a). Under the assumption that there are no significant changes in lithology, the Poisson's ratio should increase to values close to 0.5 as saturation approaches 310 100%. In our data, the Poisson's ratio increases with depth and averages out to a value of ~0.46 below an elevation of 5 m a.m.s.l. (Figure 6a). An anomaly occurs between 60 to 80 m along the profile and is the only location where high Poisson's ratios (> 0.4) reach the surface. This observation is not surprising given that this profile is driven by P-wave and S-wave profiles where at 60-80 meters along the profile we observed a drop in S-wave velocities, while the P-wave velocities increased slightly (Figures 2 and 3). Because the difference in P-wave and S-wave velocity is larger, the Poisson's ratio is also larger 315 (Eq. 1).

To estimate a value of Poisson's ratio that represents the water table, we laterally averaged two regions along the profile to produce two 1D profiles with standard deviations. The standard deviations represent the lateral variability. The first laterally averaged region was between 60-80 m, where the large anomaly occurs and where higher values of Poisson's ratio reach the surface (Figure 6a). The second region was chosen to be from 120 to 220 m because qualitatively it appears laterally

320   uniform and includes the drillhole location (drillhole located at 220 m). These two averaged 1D profiles, when plotted side-by-side, show a similar trend of increasing Poisson's ratio (Figure 6c) but present a clear offset. Near the surface the difference is largest, but the two curves begin to converge near the manual water level measurement of 6.8 m and the highest water contents from the NMR (Figure 6c). At the inferred water table, the values of Poisson's ratio between 60-80 m and 120-220 m are 0.454 ± 0.004 and 0.475 ± 0.002, respectively (Figure 6b). Here we use a value of 0.46 as the contour that represents the

325   water table, which we refer to as the geophysically inferred water table depth. The value of 0.45 also validated against the manual water level measurements (6.8 m depth below ground) and the downhole NMR water content profile from the drill hole (occurring at 220 m along the profile). It also corresponds well with previous values given by Pasquet et al. (2015a, b).

Under the assumption of a flat-water table from the drillhole, the contour value of 0.46 matches qualitatively the depth to water between 0-60 m and again between 80 and 220 m (Figure 6a). There is one notable deviation occurring between

330   60-80 m where we highlight anomalies in all three geophysical methods. We observed a slight increase in P-wave velocities (Figure 2), slightly lower S-wave velocities (Figure 3), and a resistive feature in the NanoTEM data (Figure 4). As a result, the geophysically inferred water table depth at this location along the profile differs from the manually measured water level (Figure 6a). We interpret this rise in Poisson's ratios as the water table rising toward the surface beneath the subtle topographic depression in the landscape representing the ephemeral drainage feature (Figure 6b).

335   Using a contour value of 0.46 provides an estimate for the water table, but the boundary is fuzzy and possibly transitional (Figure 6a). The fuzziness of the boundary could be explained by two processes. First, partial saturation could be occurring above the water table. Second, the water table boundary could be well defined, but it is smoothed over by the geophysical inversions. The smoothing is difficult to quantify and is complicated by the fact that the P-wave and S-wave velocities come from two different inversions based on different physics. More research is needed to understand and compare

340   the sample volumes of the travel-time tomography and surface wave inversions. We gravitate the interpretation of a transitional zone between unsaturated and saturated sediments because of observations in the NMR data (Figure 5) and the presence of water measured in the samples (Figure 6c).

In the downhole NMR data, we are confident with measured water contents greater than 0.05 m^3/m^3. At 4 m depth the water content is well above 0.05 m^3/m^3 and shows a linear increase until a maximum value of 0.25 m^3/m^3 is reached

345   between 6.75 and 7.0 m below the surface (Figure 5). Below the water table, the maximum water content likely represents total porosity. All the NMR responses above the water table have low T_2 decay times (Figure 5b), which can either be indicative of clay or caused by small pores which preferentially fill and hold water after being drained (i.e. leading to partial saturation of the medium) (Walsh et al., 2014). The preferentially filled pores seems more likely because we know that the measurements were made within the vadose zone and the measured gravimetric water contents of the drillhole core showed that samples

350   retained water. The most important observation provided by the NMR data is that partially saturated sediments exist at least 3 m above the water table (Figure 6c). This partially saturated region of sediments above the water table could be the capillary fringe. This partially saturated region of the soil profile will likely increase the Poisson's ratios and provides an explanation for the transitional and fuzzy boundary we observe in the seismic data. Furthermore, if the 0.46 contour is shifted upward 3 m based on the NMR observation, it qualitatively matches the point where the Poisson's ratio begins to increase (Figure 6a).

355   From the combined interpretation of seismic data, manual water level measurement, and NMR data, we are therefore able to identify a mound in the water table underneath the small topographic depression existing between 60-80 m along the profile (Figure 6b). The NMR data and Poisson's ratio suggest the existence of a ~3 m thick section of partially saturated sediments on top of the water table along the profile (Figure 6b).

5.2 Geophysically Identified Recharge Processes

360   In the previous section we relied heavily on the seismic data and NMR data to define a geophysically inferred water table depth along the study transect (Figure 6b). We argued for the existence of a 3 m thick partially saturated region above the water table based on water contents from the NMR data (Figure 6c). In this section we utilize the bulk electrical conductivities obtained from the NanoTEM data to strengthen the interpretation that the anomaly between 60 to 80 m along the transect is caused by an increase in saturation and that the subtle topographic surface depression acts as a localized recharge

365   zone (Figure 4).

      Ambiguities exist in geophysical measurements because they measure physical properties that are related to the processes that we are trying to understand. It is for instance possible that the region of high Poisson's ratios are a result of higher clay content since materials that are deformed easily will have higher Poisson's ratios. The Poisson's ratio for pure quartz, a stiff mineral, is between 0.06 and 0.08, Kaolinite is 0.14, and clays are around 0.34 and 0.35 (Mavko et al., 2009). It

370   would be reasonable to assume higher clay content as an alternative interpretation to explain the higher Poisson's ratios under the topographic surface depression. Here the conductivities from the NanoTEM provide evidence to suggest that an increase in clay content is unlikely. If the high Poisson's ratio were due to an increased clay content, we would expect the electrical conductivities to rise—but we observe the opposite. The subsurface is more resistive at the location where the Poisson's ratios rise.

375   Underneath the small depression in topography between 60-80 m along the seismic profile we have anomalies in all three geophysical data sets: 1) the P-wave velocities increase, 2) the S-wave velocities decrease, and 3) the electrical conductivities decrease. As discussed in the previous section, the first two anomalies cause the Poisson's ratio to rise, which we interpret as a rise of the water table, or at least an increase in water saturation. Here we believe the decrease in electrical conductivity is the result of more conductive groundwater being replaced by fresher water that has infiltrated from rainfall

380   events. The electrical conductivity of the formation (the one that we measure) can be modelled using Archie's Law (Archie, 1941; Robinson et al., 2012).

$$R_{form} = \phi^{-m} S^{-n} R_{fluid},\tag{2}$$

In Eq. 2 φ is porosity, S is saturation, R_{form} is the formation resistivity, R_{fluid} is the fluid resistivity, and conductivity is the inverse of resistivity. The variable m is the cementation coefficient, which accounts for effects of permeability and

385 tortuosity. This value varies between 1.2 and 4.4 (Lesmes and Friedman, 2005; Robinson et al., 2012). The variable n is an empirically defined coefficient but is commonly set at a value of 2 (Day-Lewis, 2005; Knight, 1991; Robinson et al., 2012). Using Archie's equation (Eq. 2) we can explore how the conductivity of the formation will respond as a function of fluid saturation and the conductivity of the fluid. It is often assumed that as the water saturation increases, the fluid conductivity will also increase. We used Archie's law to show that it is possible to observe a drop in electrical conductivity if the pores are

390 being saturated with a more resistive fluid or if a less conductive fluid replaces the higher conductive fluid originally in place.

Although we did not measure the electrical conductivity of rain water, we know that the groundwater conductivity is high (14750 μS·cm^{-1}). Therefore, we assume that the electrical conductivity of the groundwater will be higher than that of rain water. The assumption is further justified because salinities in the shallow quaternary systems range between 2000 and 13,000 mg·L^{-1} (Department for Water, 2010). Using the fully saturated volumetric water content below the water table from the

395 downhole NMR data provides an estimated porosity of 0.25 m^3/m^3 (Figure 5d). Assuming a soil density of 1.5 provides a porosity estimate of 0.23 m^3/m^3 from the soil samples collected, which is consistent with the NMR results (Figure 5a). Using equation 2, we calculated the electrical conductivity assuming a fixed porosity of 0.25 m^3/m^3, setting m to 1.3, setting n to 2, and varying the fluid conductivity from 500 to 4000 mS.m^{-1} and a saturation from 0 to 1 m^3/m^3 (Figure 7a).

There are three end-member cases that can be observed from the calculation of the formation conductivity (Figure

400 7a). The first is filling the pores with water that has the same electrical conductivity as the groundwater (Figure 7a). The result is that the formation conductivity rises exponentially (Figure 7b) and this is consistent with the common interpretation that increasing the saturation also increases the electrical conductivity. The second case is filing the pores with saltier water; that is the fluid filling the pore-space has an increasingly higher electrical conductivity. In this case the formation conductivity also rises exponentially, but at an even faster rate than just filling the pores with water (Figure 7b). The last end member case is

405 filling the pores with fresher water. That is as the saturation increases the fluid conductivity decreases. In this case, it is possible to get a small drop in electrical conductivities (Figure 7b). Furthermore, from this relationship it can be observed that at the same saturation level, the formation conductivity will reduce if the fluid in the pore space is replaced with a more resistive fluid (Figure 7a). This basic forward modelling exercise shows that if we replace the water in the pores with a more resistive fluid, it is possible to get a drop in electrical conductivity.

410

5.3 Hydrogeological Implications

We combine all the geophysical observations to construct a hydrogeological interpretation (Figure 8). First, based on the seismic data and the measured water depth from the nearby drillhole we can identify a rise in the water table underneath the small topographic depression. It is likely that this rise in water table has a partially saturated region that is ~3 m thick above

415 it. Because the observed drop in electrical conductivities, we interpret this feature as a saturation increase and not a change

increase clay content. We interpret the drop in electrical conductivities as fresher water replacing the ambient saline groundwater of the Quaternary aquifer. The resistive feature lies above the partially saturated or saturated zones between 80 and 100 m and again between 120-140 m (Figure 8).

The recharge mechanisms and processes occurring across the NAP are complex and not well understood. Hydraulic head, chloride, and electrical conductivity data have been used to suggest that the major recharge mechanism of the Quaternary and Tertiary aquifers is surface water infiltration along the large rivers in the NAP; namely the Gawler and Light river systems (Bresciani et al., 2018). In another study, environmental tracers, stable isotopes, and age groundwater age dating were used to argue that although recharge into the Quaternary system occurs through infiltration along rivers, they argue that there is limited connection to the underlying Tertiary aquifers and that recharge occurs through lateral groundwater flow from the Mount Lofty Ranges (Batlle-Aguilar et al., 2017). Our study has shown that the smaller tributaries and ephemeral streams are acting as localized sources for recharge into the Quaternary and Tertiary aquifer implying localized recharge across the NAP—an interpretation consistent with the finding of Bresciani et al. (2018) and one that has major consequences for the overall conceptualization and management of the aquifer systems in this region.

It should be noted that our hydrogeological interpretation is based on a single snap shot in time. Without time-lapse geophysical measurements, groundwater samples taken from within the groundwater mound and either side, or long-term monitoring of groundwater observations wells, it is not possible to definitively quantify the recharge rates in these systems. Nor is it possible to determine if the groundwater mound is a result of a recent rainfall event or if it is a more stable feature. It seems reasonable, given the evidence of ephemeral surface drainage features in the LiDAR data (Figure 1d) and the high clay content of the near-subsurface that surface water would flow towards subtle depressions in the landscape and eventually out to St Vincent Gulf (Figure 8). These small ephemeral features are unmonitored, so it is unknown how quickly or how much water flows through them during storm events. The NAP is topographically flat so it is possible that instead of surface water flowing out towards the ocean, it might accumulate water in these low-lying features after large rainfall or storm events and gradually infiltrate over longer periods of times. The ponded water from such rainfall events would produce localized recharge to the underlying aquifer system (Figure 8). The recharge water would be fresher than the groundwater already in the Quaternary aquifer system.

The hydrological conceptualization based on the geophysical data (Figure 8) could be confirmed or rejected by drilling and sampling the groundwater via an additional shallow drill hole across the shallow topographic depression—but it would have been impossible to know this ahead of time. The unique combination of geophysical data has provided a new perspective that allows us to speculate about important local hydrological processes taking place in the NAP. Furthermore, the conceptualization can be used to guide and plan detailed investigations centralized on understanding the role of these subtle depressions across this flat semi-arid landscape. We believe that the combined geophysical approach provided a vital conceptual framework for the hydrological processes occurring within the area. Future work should focus on combining the geophysical measurements with more traditional hydrological and geochemical measurements to fully explore and test the

hydrogeological conceptualization suggested in this manuscript and the transient nature of the recharge mechanisms (Figure
450   8).

5.4 Applying the Combined Geophysical Approach to other Semi-arid Regions

Throughout this study we used well established geophysical methods. Each of these methods have open source
inversions available or the equipment comes with easy to use inversion software. Thus, there is nothing novel about the
processing of each individual geophysical dataset. The novelty comes from the unique combination of all these methods to
455   build a new conceptual model of the recharge processes in a flat lying semi-arid landscape. In order to facilitate and expand
the use of this combined geophysical approach to other semi-arid streams or features, we highlight some of the uncertainty,
limitations, advantages, and critical assumptions that went into building the hydrological conceptualization so that this
methodology might be transferred to other semi-arid areas that are common around the world.

We relied heavily on the manual water level measurement and downhole NMR data. The geophysical mapped water
460   table essentially extended from the water level that we were able to measure at the drillhole location. The drillhole data were
critical to calibrate the value of Poisson's ratio that we used to represent the water table. The method would be much more
powerful if the drillhole was not required, but because this was the first survey of its kind in the region we needed to confirm
where the water level was to interpret the Poisson's ratio. Now, with value of 0.45 it would be possible to run a survey without
the drillhole and predict the water level without a drillhole. Thus, some validation is required prior to extending the
465   methodologies throughout the NAP.

The NAP provided ideal conditions for us to exploit Poisson's ratio to map the water table in detail. The NAP was
ideal because the subsurface was broadly homogeneous, and there were no abrupt or lateral variations in the lithology.
Lithological variation would complicate the interpretation of the Poisson's ratio because all the changes could not be attributed
solely to changes in saturation. We were also specific in selecting a location where the water table was between 3 and 10 m
470   depth. In order to image the saturated zone with seismic methodologies, we required an elastic contrast between the unsaturated
and saturated zones. Although uncertainty is difficult to quantify given the different sample volumes and wavelengths of the
seismic wave field and Rayleigh waves (work that extends beyond the scope of this paper) we believe that having at least three
meters of unsaturated zone above the water table should provide a strong enough contrast to image. Furthermore, the inversion
of surface waves is limited by the frequency content of the source and the peak geophone frequency. In our case, with 14 Hz
475   geophones, imaging a water table that is below ~10-12 meters would be difficult. Thus, to improve chances of success, the
seismic approach should be applied in regions where the water table is between 3-10 m in a homogeneous material.

The additional information provided by the NanoTEM data helped reduce ambiguities observed in the Poisson's ratio
profile. Without this additional information it would have been difficult to determine if the anomaly was caused by an increased
clay content or an increase in water content. Thus, the electrical conductivity data was critical to our hydrological interpretation.
480   It should be noted that the NanoTEM data could also be replaced by another independent observation e.g. other near surface

geophysical methods or soil conductivity profiles at several locations along the transect. Regardless, more observational evidence, even if they are point measurements, will aid in the interpretation of the geophysical images.

6 Conclusions

485   We have shown that the unique combination of P-wave and S-wave velocities, electrical conductivities, and surface NMR can identify small-scale ephemeral recharge features in a semi-arid landscape without time-lapse measurements. The seismic data were used as the foundation to geophysically infer the water table depth, the NMR data showed a 3 m thick region of partially saturated sediments, and the electrical conductivities from the NanoTEM provided information about the fluid within the pore space. The combination of all four data sets has provided a hydrogeological framework where we are observing fresher water recharging and replenishing the underlying saline Quaternary aquifer system. Although the timing or flux rates

490   of the recharge cannot be determined with our data, we have shown that small scale ephemeral features likely play a vital role in recharge mechanisms to the shallow unconfined aquifers of the low-lying semi-arid landscape of the NAP. The interpretation of the geophysical data still requires more traditional hydrogeological measurements to test, but we have demonstrated that unique, spatially exhaustive perspective gained using near-surface geophysical methods can be valuable to understanding the recharge processes and conceptualization of semi-arid hydrological systems.

495   ## 7 Acknowledgments

We would like to thank Adrian Costar for help in collection of the seismic data set. We acknowledge funding from the Goyder Institute for Water Research for the project ED-17-01, 'Sustainable expansion of irrigated agriculture and horticulture in Northern Adelaide Corridor: Task 4 – assessment of depth to groundwater (proof of concept)'. We are grateful for the land access provided by John Gordon. We would also like to thank Chris Li and Sebastian Lamontagne for providing valuable

500   comments that improved the manuscript.

References

Abdulrazzak, M. J.: Losses of flood water from alluvial channels, Arid Soil Research and Rehabilitation, 9(1), 15–24, doi:10.1080/15324989509385870, 1995.

Acuña, V., Datry, T., Marshall, J., Barceló, D., Dahm, C. N., Ginebreda, A., McGregor, G., Sabater, S., Tockner, K. and
505   Palmer, M. A.: Why Should We Care About Temporary Waterways?, Science, 343(6175), 1080–1081, doi:10.1126/science.1246666, 2014.

Allison, G. B., Cook, P. G., Barnett, S. R., Walker, G. R., Jolly, I. D. and Hughes, M. W.: Land clearance and river salinisation in the western Murray Basin, Australia, Journal of Hydrology, 119(1), 1–20, doi:10.1016/0022-1694(90)90030-2, 1990.

Anderson, T. A., Bestland, E. A., Wallis, I. and Guan, H. D.: Salinity balance and historical flushing quantified in a high-rainfall catchment (Mount Lofty Ranges, South Australia), Hydrogeol J, doi:10.1007/s10040-018-01916-7, 2019.

Archie, G. E.: The Electrical Resistivity Log as an Aid in Determining Some Reservoir Characteristics, Transactions of the American Institute of Mining and Metallurgical Engineers, 146, 54–61, 1941.

Auken, E., Pellerin, L., Christensen, N. B. and Sørensen, K.: A survey of current trends in near-surface electrical and electromagnetic methods, GEOPHYSICS, 71(5), G249–G260, doi:10.1190/1.2335575, 2006.

Auken, E., Christiansen, A. V., Kirkegaard, C., Fiandaca, G., Schamper, C., Behroozmand, A. A., Binley, A., Nielsen, E., Effersø, F., Christensen, N. B., Sørensen, K., Foged, N. and Vignoli, G.: An overview of a highly versatile forward and stable inverse algorithm for airborne, ground-based and borehole electromagnetic and electric data, Exploration Geophysics, 46(3), 223–235, doi:10.1071/EG13097, 2015.

Bachrach, R. and Nur, A.: High-resolution shallow-seismic experiments in sand, Part I: Water table, fluid flow, and saturation, Geophysics, 63(4), 1225–1233, doi:10.1190/1.1444423, 1998.

Bachrach, R., Dvorkin, J. and Nur, A.: Seismic velocities and Poisson's ratio of shallow unconsolidated sands, Geophysics, 65(2), 559–564, doi:10.1190/1.1444751, 2000.

Banks, E. W., Simmons, C. T., Love, A. J., Cranswick, R., Werner, A. D., Bestland, E. A., Wood, M. and Wilson, T.: Fractured bedrock and saprolite hydrogeologic controls on groundwater/surface-water interaction: a conceptual model (Australia), Hydrogeol J, 17(8), 1969–1989, doi:10.1007/s10040-009-0490-7, 2009.

Banks, E. W., Simmons, C. T., Love, A. J. and Shand, P.: Assessing spatial and temporal connectivity between surface water and groundwater in a regional catchment: Implications for regional scale water quantity and quality, Journal of Hydrology, 404(1), 30–49, doi:10.1016/j.jhydrol.2011.04.017, 2011.

Batlle-Aguilar, J., Banks, E. W., Batelaan, O., Kipfer, R., Brennwald, M. S. and Cook, P. G.: Groundwater residence time and aquifer recharge in multilayered, semi-confined and faulted aquifer systems using environmental tracers, Journal of Hydrology, 546, 150–165, doi:10.1016/j.jhydrol.2016.12.036, 2017.

Behroozmand, A. A., Keating, K. and Auken, E.: A Review of the Principles and Applications of the NMR Technique for Near-Surface Characterization, Surveys in Geophysics, 36(1), 27–85, doi:10.1007/s10712-014-9304-0, 2015.

Berryman, J. G., Berge, P. A. and Bonner, B. P.: Estimating rock porosity and fluid saturation using only seismic velocities, Geophysics, 67(2), 391–404, doi:10.1190/1.1468599, 2002.

Bertin, Clotilde. and Bourg, A. C. M.: Radon-222 and Chloride as Natural Tracers of the Infiltration of River Water into an Alluvial Aquifer in Which There Is Significant River/Groundwater Mixing, Environ. Sci. Technol., 28(5), 794–798, doi:10.1021/es00054a008, 1994.

Bloch, F.: Nuclear Induction, Phys. Rev., 70(7–8), 460–474, doi:10.1103/PhysRev.70.460, 1946.

Bresciani, E., Cranswick, R. H., Banks, E. W., Batlle-Aguilar, J., Cook, P. G. and Batelaan, O.: Using hydraulic head, chloride and electrical conductivity data to distinguish between mountain-front and mountain-block recharge to basin aquifers, Hydrol. Earth Syst. Sci., 22(2), 1629–1648, doi:10.5194/hess-22-1629-2018, 2018.

Brownstein, K. R. and Tarr, C. E.: Importance of classical diffusion in NMR studies of water in biological cells, Phys. Rev. A, 19(6), 2446–2453, doi:10.1103/PhysRevA.19.2446, 1979.

545   Brunner, P., Simmons, C. T. and Cook, P. G.: Spatial and temporal aspects of the transition from connection to disconnection between rivers, lakes and groundwater, Journal of Hydrology, 376(1), 159–169, doi:10.1016/j.jhydrol.2009.07.023, 2009.

Carey, A. M. and Paige, G. B.: Ecological Site-Scale Hydrologic Response in a Semiarid Rangeland Watershed, Rangeland Ecology & Management, doi:10.1016/j.rama.2016.06.007, 2016.

Chapman, T.: A comparison of algorithms for stream flow recession and baseflow separation, Hydrological Processes, 13(5),
550   701–714, doi:10.1002/(SICI)1099-1085(19990415)13:5<701::AID-HYP774>3.0.CO;2-2, 1999.

Claes, N., Paige, G. B. and Parsekian, A. D.: Uniform and lateral preferential flows under flood irrigation at field scale, Hydrological Processes, 0(0), doi:10.1002/hyp.13461, 2019.

Coates, G. R., Xiao, L. and Prammer, M. G.: NMR logging principles and applications, Halliburton Energy Services, United States., 1999.

555   Cohen, M. H. and Mendelson, K. S.: Nuclear magnetic relaxation and the internal geometry of sedimentary rocks, Journal of Applied Physics, 53(2), 1127–1135, doi:10.1063/1.330526, 1982.

Cook, P. G., Solomon, D. K., Sanford, W. E., Busenberg, E., Plummer, L. N. and Poreda, R. J.: Inferring shallow groundwater flow in saprolite and fractured rock using environmental tracers, Water Resour. Res., 32(6), 1501–1509, doi:10.1029/96WR00354, 1996.

560   Crosbie, R. S., Peeters, L. J. M., Herron, N., McVicar, T. R. and Herr, A.: Estimating groundwater recharge and its associated uncertainty: Use of regression kriging and the chloride mass balance method, Journal of Hydrology, 561, 1063–1080, doi:10.1016/j.jhydrol.2017.08.003, 2018.

Cuthbert, M. O., Acworth, R. I., Andersen, M. S., Larsen, J. R., McCallum, A. M., Rau, G. C. and Tellam, J. H.: Understanding and quantifying focused, indirect groundwater recharge from ephemeral streams using water table fluctuations, Water
565   Resources Research, 52(2), 827–840, doi:10.1002/2015WR017503, 2016.

Dahan, O., Shani, Y., Enzel, Y., Yechieli, Y. and Yakirevich, A.: Direct measurements of floodwater infiltration into shallow alluvial aquifers, Journal of Hydrology, 344(3), 157–170, doi:10.1016/j.jhydrol.2007.06.033, 2007.

Dahan, O., Tatarsky, B., Enzel, Y., Kulls, C., Seely, M. and Benito, G.: Dynamics of Flood Water Infiltration and Ground Water Recharge in Hyperarid Desert, Groundwater, 46(3), 450–461, doi:10.1111/j.1745-6584.2007.00414.x, 2008.

570   Day-Lewis, F. D.: Applying petrophysical models to radar travel time and electrical resistivity tomograms: Resolution-dependent limitations, J. Geophys. Res., 110(B8), B08206, doi:10.1029/2004JB003569, 2005.

Department for Water: Northern Adelaide Plains PWA Groundwater Level and Salinity Status Report 2009-2010, Government of South Australia, Adelaide, South Australia., 2010.

Desper, D. B., Link, C. A. and Nelson, P. N.: Accurate water-table depth estimation using seismic refraction in areas of rapidly
575   varying subsurface conditions, Near Surface Geophysics, 13(2096), doi:10.3997/1873-0604.2015039, 2015.

Dijkstra, E. W.: A note on two problems in connexion with graphs, Numer. Math., 1(1), 269–271, doi:10.1007/BF01386390, 1959.

Dunn, K. J., Bergman, D. J. and LaTorraca, G. A.: Nuclear Magnetic Resonance: Petrophysical and Logging Applications, Elsevier., 2002.

580   Dvorkin, J. and Nur, A.: Elasticity of high-porosity sandstones: Theory for two North Sea data sets, Geophysics, 61(5), 1363–1370, doi:10.1190/1.1444059, 1996.

Earman, S., Campbell, A. R., Phillips, F. M. and Newman, B. D.: Isotopic exchange between snow and atmospheric water vapor: Estimation of the snowmelt component of groundwater recharge in the southwestern United States, Journal of Geophysical Research: Atmospheres, 111(D9), doi:10.1029/2005JD006470, 2006.

585   Flinchum, B. A., Holbrook, W. S., Rempe, D., Moon, S., Riebe, C. S., Carr, B. J., Hayes, J. L., Clair, J. and Peters, M. P.: Critical Zone Structure Under a Granite Ridge Inferred From Drilling and Three-Dimensional Seismic Refraction Data, Journal of Geophysical Research: Earth Surface, 123(6), 1317–1343, doi:10.1029/2017JF004280, 2018.

Genereux, D. P. and Hemond, H. F.: Naturally Occurring Radon 222 as a Tracer for Streamflow Generation: Steady State Methodology and Field Example, Water Resources Research, 3065–3075,
590   doi:10.1029/WR026i012p03065@10.1002/(ISSN)1944-7973.CHAPMAN5, 2010.

Gleeson, T., Wada, Y., Bierkens, M. F. P. and van Beek, L. P. H.: Water balance of global aquifers revealed by groundwater footprint, Nature, 488(7410), 197–200, doi:10.1038/nature11295, 2012.

Gottschalk, I. P., Hermans, T., Knight, R., Caers, J., Cameron, D. A., Regnery, J. and McCray, J. E.: Integrating non-colocated well and geophysical data to capture subsurface heterogeneity at an aquifer recharge and recovery site, Journal of Hydrology,
595   555(Supplement C), 407–419, doi:10.1016/j.jhydrol.2017.10.028, 2017.

Gregory, A. R.: Fluid saturation effects on dynamic elastic properties of sedimentary rocks, Geophysics, 41(5), 895–921, doi:10.1190/1.1440671, 1976.

Grunewald, E. and Knight, R.: Nonexponential decay of the surface-NMR signal and implications for water content estimation, GEOPHYSICS, 77(1), EN1–EN9, doi:10.1190/geo2011-0160.1, 2012.

600   Hashin, Z. and Shtrikman, S.: A variational approach to the theory of the elastic behaviour of multiphase materials, Journal of the Mechanics and Physics of Solids, 11(2), 127–140, doi:10.1016/0022-5096(63)90060-7, 1963.

Hoehn, E. and Gunten, H. R. V.: Radon in groundwater: A tool to assess infiltration from surface waters to aquifers, Water Resources Research, 25(8), 1795–1803, doi:10.1029/WR025i008p01795, 1989.

Johnson, T. C., Slater, L. D., Ntarlagiannis, D., Day-Lewis, F. D. and Elwaseif, M.: Monitoring groundwater-surface water
605   interaction using time-series and time-frequency analysis of transient three-dimensional electrical resistivity changes, Water Resources Research, 48(7), W07506, 2012.

Knight, R.: Hysteresis in the electrical resistivity of partially saturated sandstones, GEOPHYSICS, 56(12), 2139–2147, doi:10.1190/1.1443028, 1991.

Kotikian, M., Parsekian, A. D., Paige, G. and Carey, A.: Observing Heterogeneous Unsaturated Flow at the Hillslope Scale
610   Using Time-Lapse Electrical Resistivity Tomography, Vadose Zone Journal, 18(1), doi:10.2136/vzj2018.07.0138, 2019.

Lamontagne, S., Leaney, F. W. and Herczeg, A. L.: Groundwater–surface water interactions in a large semi-arid floodplain: implications for salinity management, Hydrological Processes, 19(16), 3063–3080, doi:10.1002/hyp.5832, 2005.

Lamontagne, S., Taylor, A. R., Cook, P. G., Crosbie, R. S., Brownbill, R., Williams, R. M. and Brunner, P.: Field assessment of surface water–groundwater connectivity in a semi-arid river basin (Murray–Darling, Australia), Hydrological Processes,
615   28(4), 1561–1572, doi:10.1002/hyp.9691, 2014.

Lesmes, D. P. and Friedman, S. P.: Relationships between the Electrical and Hydrogeological Properties of Rocks and Soils, in Hydrogeophysics, edited by Y. Rubin and S. S. Hubbard, pp. 87–128, Springer Netherlands, Dordrecht., 2005.

Levitt, M. H.: Spin Dynamics: Basics of Nuclear Magnetic Resonance, John Wiley & Sons., 2001.

Lowrie, W.: Fundamentals of Geophysics, Cambridge University Press., 2007.

620   Mavko, G., Mukerji, T. and Dvorkin, J.: The rock physics handbook tools for seismic analysis of porous media, Cambridge University Press, Cambridge, UK; New York. [online] Available from: http://site.ebrary.com/id/10313031 (Accessed 21 February 2014), 2009.

Mokhtar, T. A., Herrmann, R. B. and Russell, D. R.: Seismic velocity and Q model for the shallow structure of the Arabian Shield from short-period Rayleigh waves, Geophysics, 53(11), 1379–1387, doi:10.1190/1.1442417, 1988.

625   Moser, T.: Shortest-Path Calculation of Seismic Rays, Geophysics, 56(1), 59–67, doi:10.1190/1.1442958, 1991.

Moser, T. J., Nolet, G. and Snieder, R.: Ray bending revisited, Bulletin of the Seismological Society of America, 82(1), 259–288, 1992.

Neducza, B.: Stacking of surface wavesSSW provides high-quality dispersion, Geophysics, 72(2), V51–V58, doi:10.1190/1.2431635, 2007.

630   Nur, A. and Simmons, G.: The effect of saturation on velocity in low porosity rocks, Earth and Planetary Science Letters, 7(2), 183–193, doi:10.1016/0012-821X(69)90035-1, 1969.

O'Neil, A.: Full-waveform reflectivity for modeling, inversion and appraisal of seismic surface wave dispersion in shallow site investigations, Ph.D., University of Western Australia, Perth., 2003.

Orlando, J., Comas, X., Hynek, S. A., Buss, H. L. and Brantley, S. L.: Architecture of the deep critical zone in the Río Icacos
635   watershed (Luquillo Critical Zone Observatory, Puerto Rico) inferred from drilling and ground penetrating radar (GPR): Drilling and GPR explore weathering in the Rio Icacos LCZO watershed, Earth Surface Processes and Landforms, 41(13), 1826–1840, doi:10.1002/esp.3948, 2016.

Parasnis, D. S.: Principles of Applied Geophysics, Springer Netherlands, Dordrecht. [online] Available from: https://doi.org/10.1007/978-94-009-4113-7 (Accessed 27 June 2019), 1986.

640   Park, C. B., Miller, R. D. and Xia, J.: Multichannel analysis of surface waves, Geophysics, 64(3), 800–808, doi:10.1190/1.1444590, 1999.

Parsekian, A. D., Singha, K., Minsley, B. J., Holbrook, W. S. and Slater, L.: Multiscale geophysical imaging of the critical zone: Geophysical Imaging of the Critical Zone, Reviews of Geophysics, 53(1), 1–26, doi:10.1002/2014RG000465, 2015.

Pasquet, S. and Bodet, L.: SWIP: An integrated workflow for surface-wave dispersion inversion and profiling, Geophysics,
645   82(6), WB47–WB61, doi:10.1190/geo2016-0625.1, 2017.

Pasquet, S., Bodet, L., Longuevergne, L., Dhemaied, A., Camerlynck, C., Rejiba, F. and Guérin, R.: 2D characterization of near-surface : surface-wave dispersion inversion versus refraction tomography, Near Surface Geophysics, 13(4), 315–332, doi:10.3997/1873-0604.2015028, 2015a.

Pasquet, S., Bodet, L., Dhemaied, A., Mouhri, A., Vitale, Q., Rejiba, F., Flipo, N. and Guérin, R.: Detecting different water table levels in a shallow aquifer with combined P-, surface and SH-wave surveys: Insights from VP/VS or Poisson's ratios, Journal of Applied Geophysics, 113, 38–50, doi:10.1016/j.jappgeo.2014.12.005, 2015b.

Pasquet, S., Holbrook, W. S., Carr, B. J. and Sims, K. W. W.: Geophysical imaging of shallow degassing in a Yellowstone hydrothermal system: Imaging Shallow Degassing in Yellowstone, Geophysical Research Letters, 43(23), 12,027-12,035, doi:10.1002/2016GL071306, 2016.

Prasad, M.: Acoustic measurements in unconsolidated sands at low effective pressure and overpressure detection, Geophysics, 67(2), 405–412, doi:10.1190/1.1468600, 2002.

Rayment, G. E. and Higginson, F. R.: Australian laboratory handbook of soil and water chemical methods, Article; Article/Report, Port Melbourne : Inkata Press. [online] Available from: https://trove.nla.gov.au/version/45465694 (Accessed 27 June 2019), 1992.

Rayment, G. E. and Lyons, D. J.: Soil chemical methods: Australasia, CSIRO Publishing, Collingwood, Vic., 2011.

Raymond, P. A., Hartmann, J., Lauerwald, R., Sobek, S., McDonald, C., Hoover, M., Butman, D., Striegl, R., Mayorga, E., Humborg, C., Kortelainen, P., Dürr, H., Meybeck, M., Ciais, P. and Guth, P.: Global carbon dioxide emissions from inland waters, Nature, 503(7476), 355–359, doi:10.1038/nature12760, 2013.

Reynolds, J. M.: An introduction to applied and environmental geophysics, 2nd ed., Chichester, West Sussex : Wiley-Blackwell. [online] Available from: https://trove.nla.gov.au/version/50745015 (Accessed 27 June 2019), 2011.

Robinson, D. A., Campbell, C. S., Hopmans, J. W., Hornbuckle, B. K., Jones, S. B., Knight, R., Ogden, F., Selker, J. and Wendroth, O.: Soil Moisture Measurement for Ecological and Hydrological Watershed-Scale Observatories: A Review, Vadose Zone Journal, 7(1), 358, doi:10.2136/vzj2007.0143, 2008.

Robinson, J. L., Slater, L. D. and Schäfer, K. V. R.: Evidence for spatial variability in hydraulic redistribution within an oak–pine forest from resistivity imaging, Journal of Hydrology, 430–431, 69–79, doi:10.1016/j.jhydrol.2012.02.002, 2012.

Rücker, C., Günther, T. and Wagner, F. M.: pyGIMLi: An open-source library for modelling and inversion in geophysics, Computers & Geosciences, 109, 106–123, doi:10.1016/j.cageo.2017.07.011, 2017.

Salem, H. S.: Poisson's ratio and the porosity of surface soils and shallow sediments, determined from seismic compressional and shear wave velocities, Géotechnique, 50(4), 461–463, doi:10.1680/geot.2000.50.4.461, 2000.

Sambridge, M.: Geophysical inversion with a neighbourhood algorithm—I. Searching a parameter space, Geophys J Int, 138(2), 479–494, doi:10.1046/j.1365-246X.1999.00876.x, 1999.

Scanlon, B. R., Healy, R. W. and Cook, P. G.: Choosing appropriate techniques for quantifying groundwater recharge, Hydrogeology Journal, 10(1), 18–39, doi:10.1007/s10040-001-0176-2, 2002.

Scanlon, B. R., Keese, K. E., Flint, A. L., Flint, L. E., Gaye, C. B., Edmunds, W. M. and Simmers, I.: Global synthesis of groundwater recharge in semiarid and arid regions, Hydrological Processes, 20(15), 3335–3370, doi:10.1002/hyp.6335, 2006.

Shanafield, M. and Cook, P. G.: Transmission losses, infiltration and groundwater recharge through ephemeral and intermittent streambeds: A review of applied methods, Journal of Hydrology, 511, 518–529, doi:10.1016/j.jhydrol.2014.01.068, 2014.

Sheehan, J. R., Doll, W. E. and Mandell, W. A.: An evaluation of methods and available software for seismic refraction tomography analysis, Journal of Environmental & Engineering Geophysics, 10(1), 21–34, 2005.

685 Siemon, B., Christiansen, A. V. and Auken, E.: A review of helicopter-borne electromagnetic methods for groundwater exploration, Near Surface Geophysics, 7(5–6), 629–646, doi:10.3997/1873-0604.2009043, 2009.

Singha, K. and Gorelick, S. M.: Saline tracer visualized with three-dimensional electrical resistivity tomography: Field-scale spatial moment analysis, Water Resources Research, 41(5), n/a-n/a, doi:10.1029/2004WR003460, 2005.

Smith, M. L., Fontaine, K. and Lewis, S. J.: Regional Hydrogeological Characterisation of the St Vincent Basin, South
690 Australia: Technical report for the National Collaboration Framework Regional Hydrogeology Project, Geoscience Australia., 2015.

Smith, W. and Wessel, P.: Gridding with continuous curvature splines in tension, Geophysics, 55(3), 293–305, doi:10.1190/1.1442837, 1990.

Stein, S. and Wysession, M.: An Introduction to Seismology, Earthquakes, and Earth Structure, Wiley., 1991.

695 Taylor, C. B., Brown, L. J., Cunliffe, J. J. and Davidson, P. W.: Environmental tritium and 18O applied in a hydrological study of the Wairau Plain and its contributing mountain catchments, Marlborough, New Zealand, Journal of Hydrology, 138(1), 269–319, doi:10.1016/0022-1694(92)90168-U, 1992.

Telford, W. M. and Telford, W. M.: Applied geophysics, London; New York : Cambridge University Press. [online] Available from: https://trove.nla.gov.au/version/45412240 (Accessed 27 June 2019), 1976.

700 Thayer, D., Parsekian, A. D., Hyde, K., Speckman, H., Beverly, D., Ewers, B., Covalt, M., Fantello, N., Kelleners, T., Ohara, N., Rogers, T. and Holbrook, W. S.: Geophysical Measurements to Determine the Hydrologic Partitioning of Snowmelt on a Snow-Dominated Subalpine Hillslope, Water Resources Research, 54(6), 3788–3808, doi:10.1029/2017WR021324, 2018.

The Goyder Institute for Water Research: Northern Adelaide Plains Water Stocktake Technical Report, The Goyder Institute for Water Research, Adelaide, South Australia., 2016.

705 Torrey, H. C.: Bloch Equations with Diffusion Terms, Phys. Rev., 104(3), 563–565, doi:10.1103/PhysRev.104.563, 1956.

Uyanık, O.: The porosity of saturated shallow sediments from seismic compressional and shear wave velocities, Journal of Applied Geophysics, 73(1), 16–24, doi:10.1016/j.jappgeo.2010.11.001, 2011.

Valois, R., Galibert, P.-Y., Guerin, R. and Plagnes, V.: Application of combined time-lapse seismic refraction and electrical resistivity tomography to the analysis of infiltration and dissolution processes in the epikarst of the Causse du Larzac (France),
710 Near Surface Geophysics, 14(2110), doi:10.3997/1873-0604.2015052, 2016.

Walsh, D. O., Turner, P., Grunewald, E. D., Zhang, H., Butler, J. J., Reboulet, E., Knobbe, S., Christy, T., Lane, J. W., Johnson, C. D., Munday, T. and Fitzpatrick, A.: A Small-Diameter NMR Logging Tool for Groundwater Investigations, Groundwater, 51(6), 914–926, doi:10.1111/gwat.12024, 2013.

Walsh, D. O., Grunewald, E. D., Turner, P., Hinnell, A. and Ferre, T. P. A.: Surface NMR instrumentation and methods for
715 detecting and characterizing water in the vadose zone, Near Surface Geophysics, 12(2016), doi:10.3997/1873-0604.2013066, 2014.

Wathelet, M., Jongmans, D. and Ohrnberger, M.: Surface-wave inversion using a direct search algorithm and its application to ambient vibration measurements, Near Surface Geophysics, 2(4), 211–221, doi:10.3997/1873-0604.2004018, 2004.

720 West, N., Kirby, E., Nyblade, A. A. and Brantley, S. L.: Climate preconditions the Critical Zone: Elucidating the role of subsurface fractures in the evolution of asymmetric topography, Earth and Planetary Science Letters, 513, 197–205, doi:10.1016/j.epsl.2019.01.039, 2019.

Winograd, I. J., Riggs, A. C. and Coplen, T. B.: The relative contributions of summer and cool-season precipitation to groundwater recharge, Spring Mountains, Nevada, USA, Hydrogeology Journal, 6(1), 77–93, doi:10.1007/s100400050135, 1998.

725 Winter, T. C., Harvey, J. W., Franke, O. L. and Alley, W. M.: Ground Water and Surface Water: A Single Resource, DIANE Publishing Inc., 1998.

Xia, J., Miller, R. D. and Park, C. B.: Estimation of near-surface shear-wave velocity by inversion of Rayleigh waves, Geophysics, 64(3), 691–700, doi:10.1190/1.1444578, 1999.

Xia, J., Miller, R. D., Park, C. B. and Tian, G.: Inversion of high frequency surface waves with fundamental and higher modes, 730 Journal of Applied Geophysics, 52(1), 45–57, doi:10.1016/S0926-9851(02)00239-2, 2003.

Xie, Y., Cook, P. G., Brunner, P., Irvine, D. J. and Simmons, C. T.: When Can Inverted Water Tables Occur Beneath Streams?, Groundwater, 52(5), 769–774, doi:10.1111/gwat.12109, 2014.

Zelt, C. A., Haines, S., Powers, M. H., Sheehan, J., Rohdewald, S., Link, C., Hayashi, K., Zhao, D., Zhou, H. -w., Burton, B. L., Petersen, U. K., Bonal, N. D. and Doll, W. E.: Blind Test of Methods for Obtaining 2-D Near-Surface Seismic Velocity 735 Models from First-Arrival Traveltimes, Journal of Environmental & Engineering Geophysics, 18(3), 183–194, doi:10.2113/JEEG18.3.183, 2013.
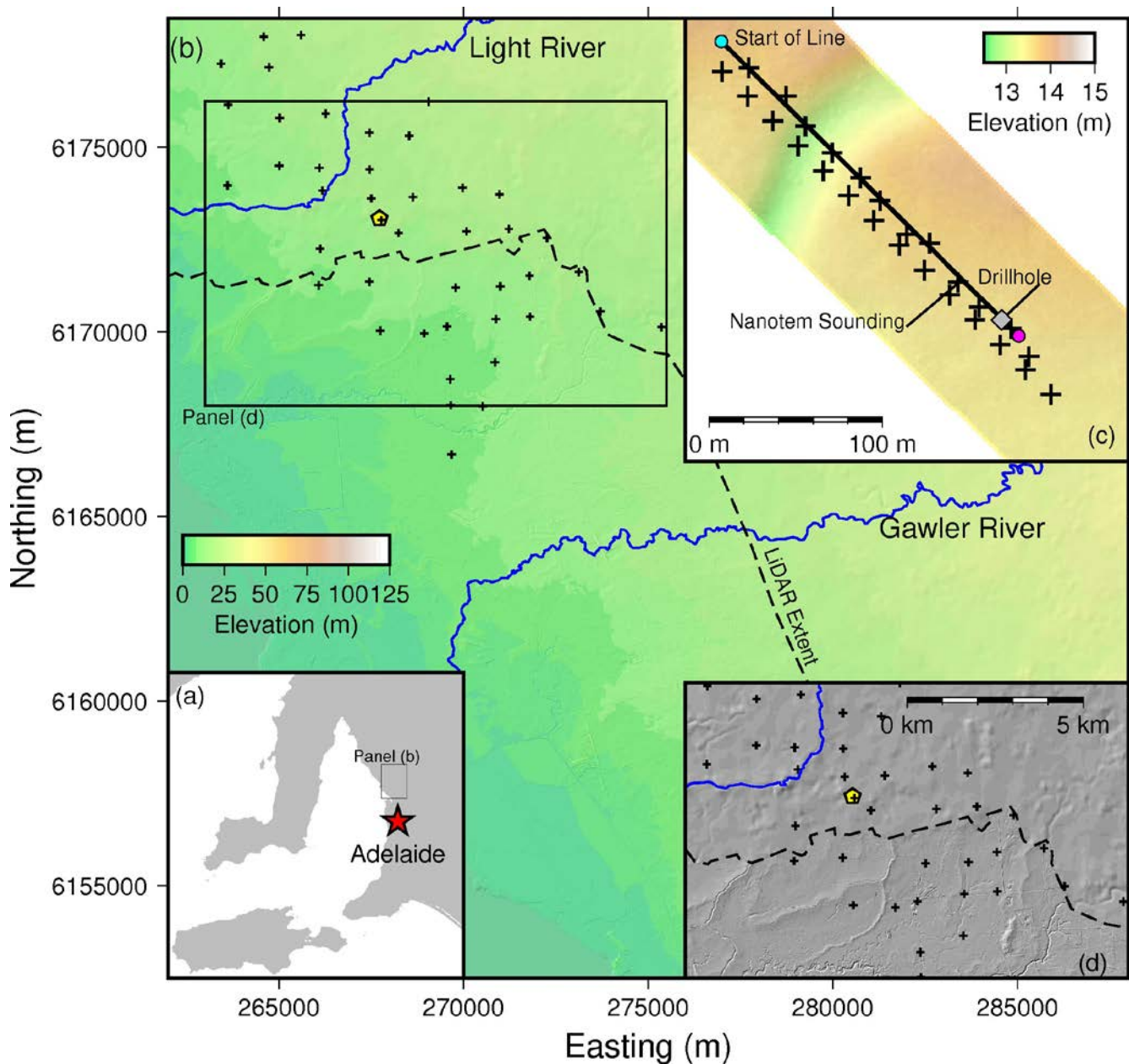
Figure 1: (a) Inset map showing the general location of the study area relative to Adelaide, South Australia. **(b)** Hillshaded
topographic relief with the LiDAR data overlaid. The northern extent of high-resolution LiDAR DEM data is marked with a dashed
line. The yellow pentagon represents the site location. Small black plus signs show the location of shallow drill holes. The Light and
Gawler Rivers are shown in blue. **(c)** High resolution topography (drone based) of the field area where the geophysical testing took
place. The thick black line is the seismic line, where the cyan dot is the start and the magenta dot is the end. Black X's represent the
location of NanoTEM soundings. The grey square is the shallow drillhole location where the downhole NMR data were collected.
(d) Inset showing two hill shaded maps of the 30 m DEM and LiDAR data. Note that additional drainage features present on the
LiDAR are not visible on the 30 m DEM data to the north of the dashed black line.
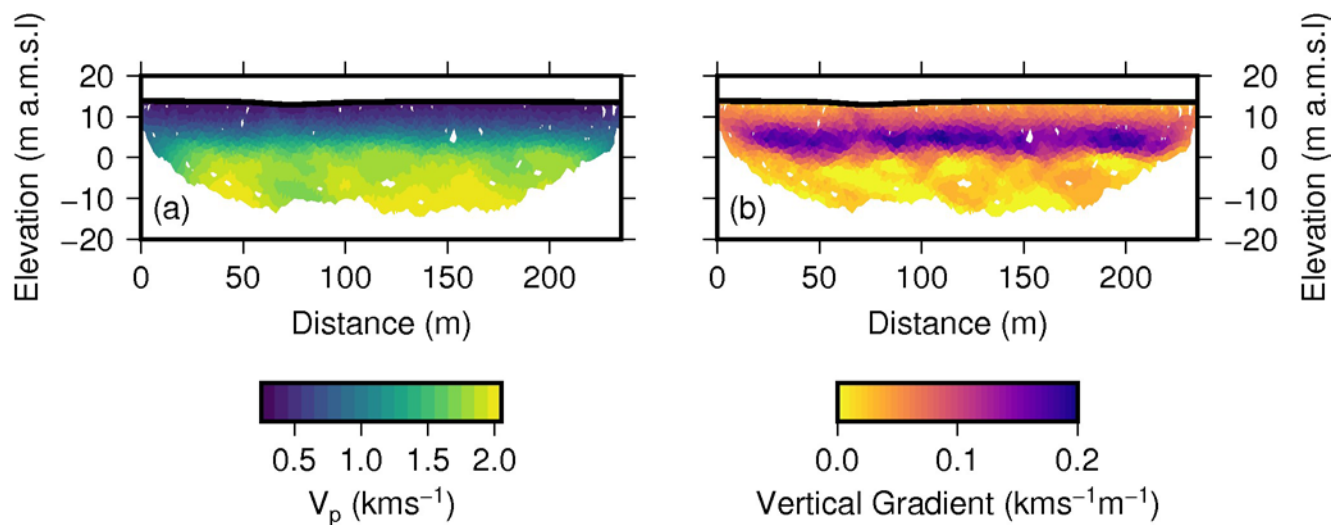
750 **Figure 2. (a) The P-wave velocity results shown at 2x vertical exaggeration. Areas where no rays pass through a model cell have been masked out. (b) The vertical velocity gradient (dv/dz) calculated from the profile shown in panel (a).**
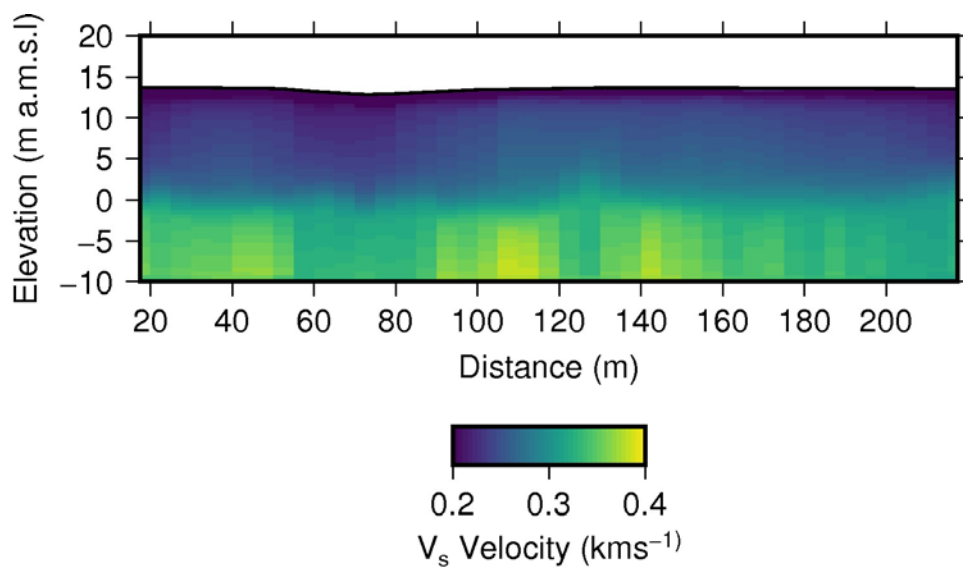
755   **Figure 3. The S-wave velocity results shown at 2x vertical exaggeration. This image shows the 42 1D inversions side-by-side; no interpolation has been applied.**
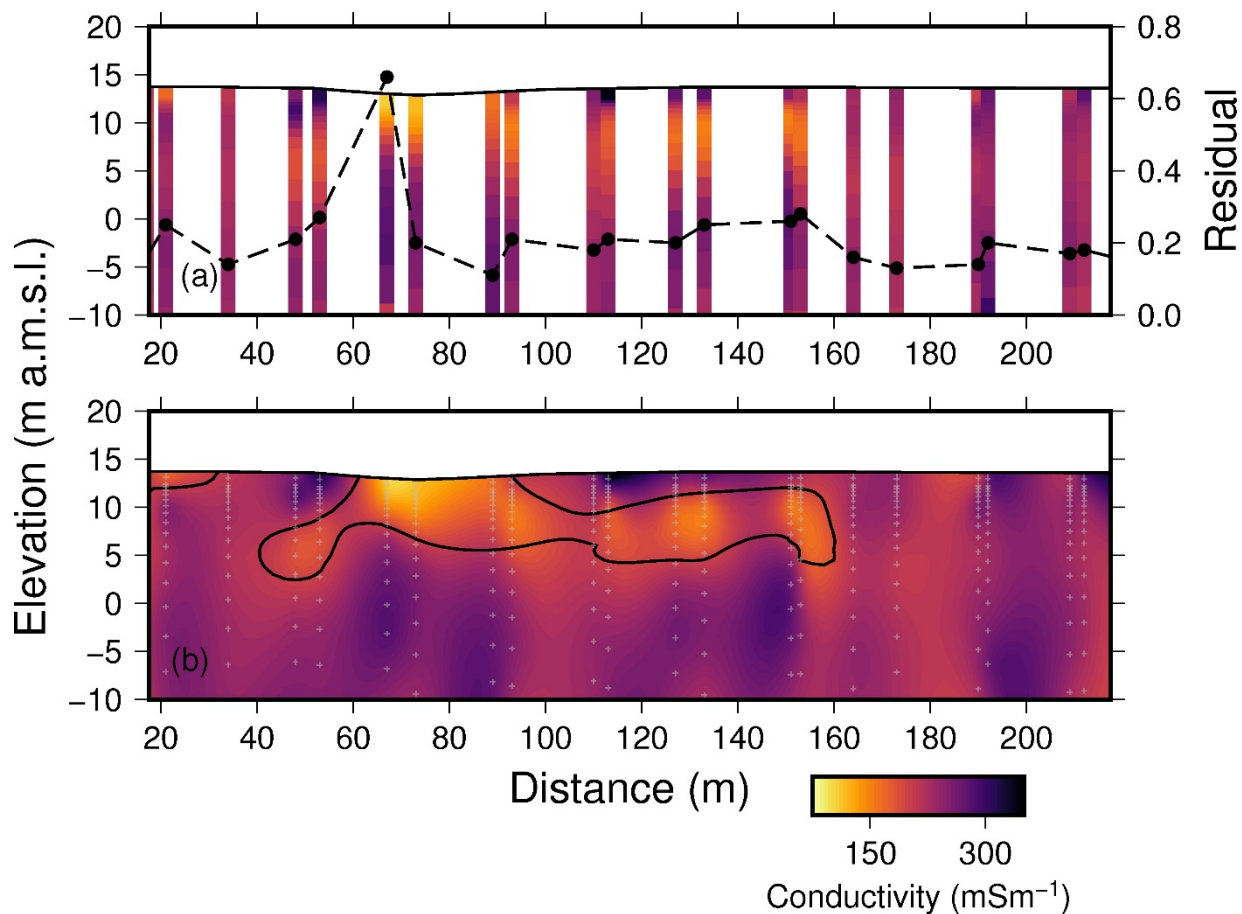
Figure 4. Electrical conductivity results produced by the NanoTEM soundings. The x-axis is distance from the first geophone (Figure 1). Both panels are shown at 2x vertical exaggeration. (a) 1D conductivity profiles plotted at their inverted resolutions as well as their spatial locations. The dots and dashed black line represent the residual between the observed and modelled decays. (b) The interpolated conductivity section. The black contour represents 200 mS·m⁻¹. The grey plus symbols represent the data used for the interpolation.

765
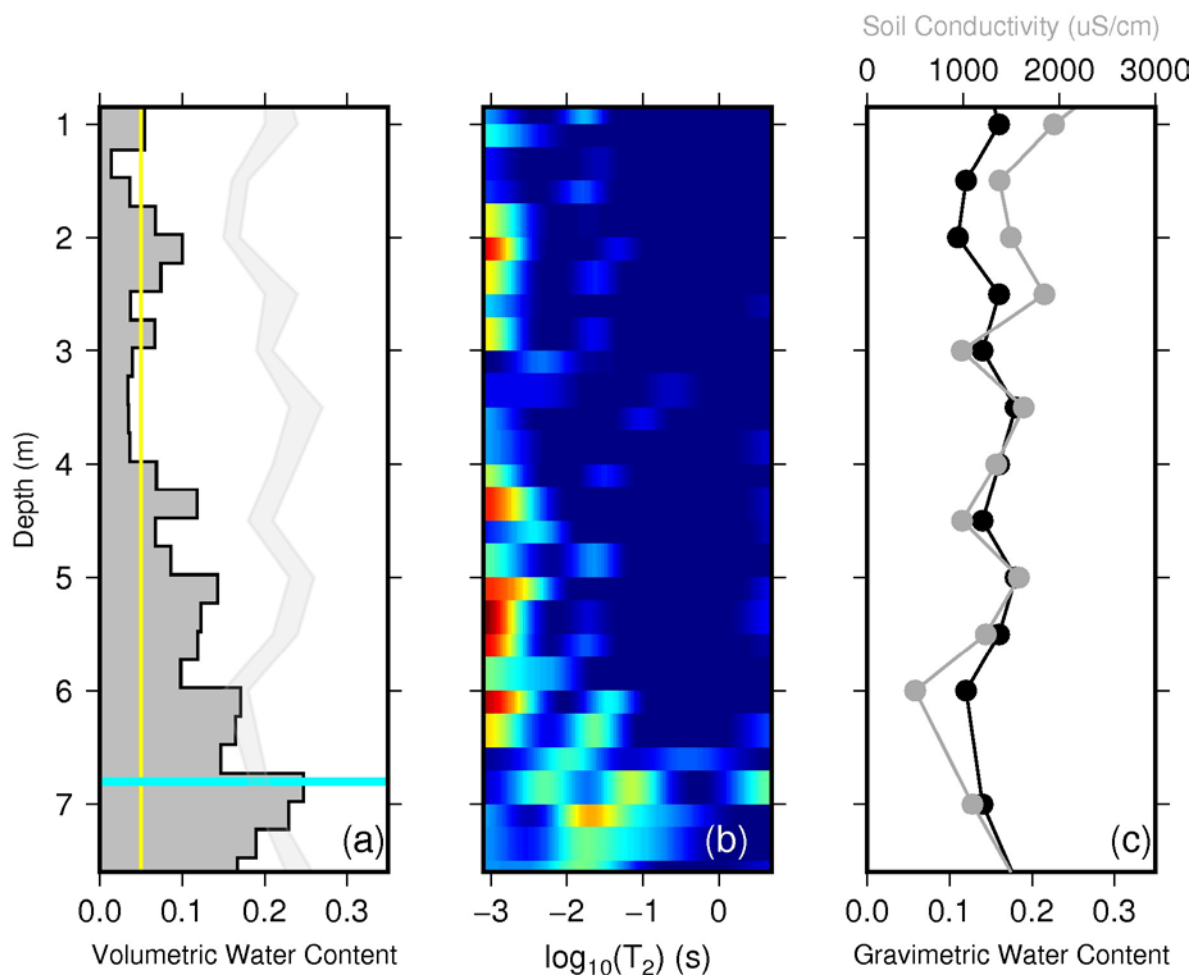
Figure 5. Results from the downhole NMR sounding and soil samples at the drillhole location (Figure 1). (a) The inverted water content profile from the downhole NMR data. The thin vertical yellow line shows the average noise level (0.05 m³/m³) below which water content estimates are questionable. The thick horizontal cyan line represents the manually measured water level (6.8 m). The
770 **thin transparent region is the volumetric water content estimated from the measured gravimetric water content, assuming a soil density between 1.3 and 1.5 g cm³. (b) The T₂ distributions that produced the water content curves in panel (a). The maximum water contents are calculated by summing the area under the distribution. (c) Soil conductivity (grey) and gravimetric water contents (black) as a function of depth.**
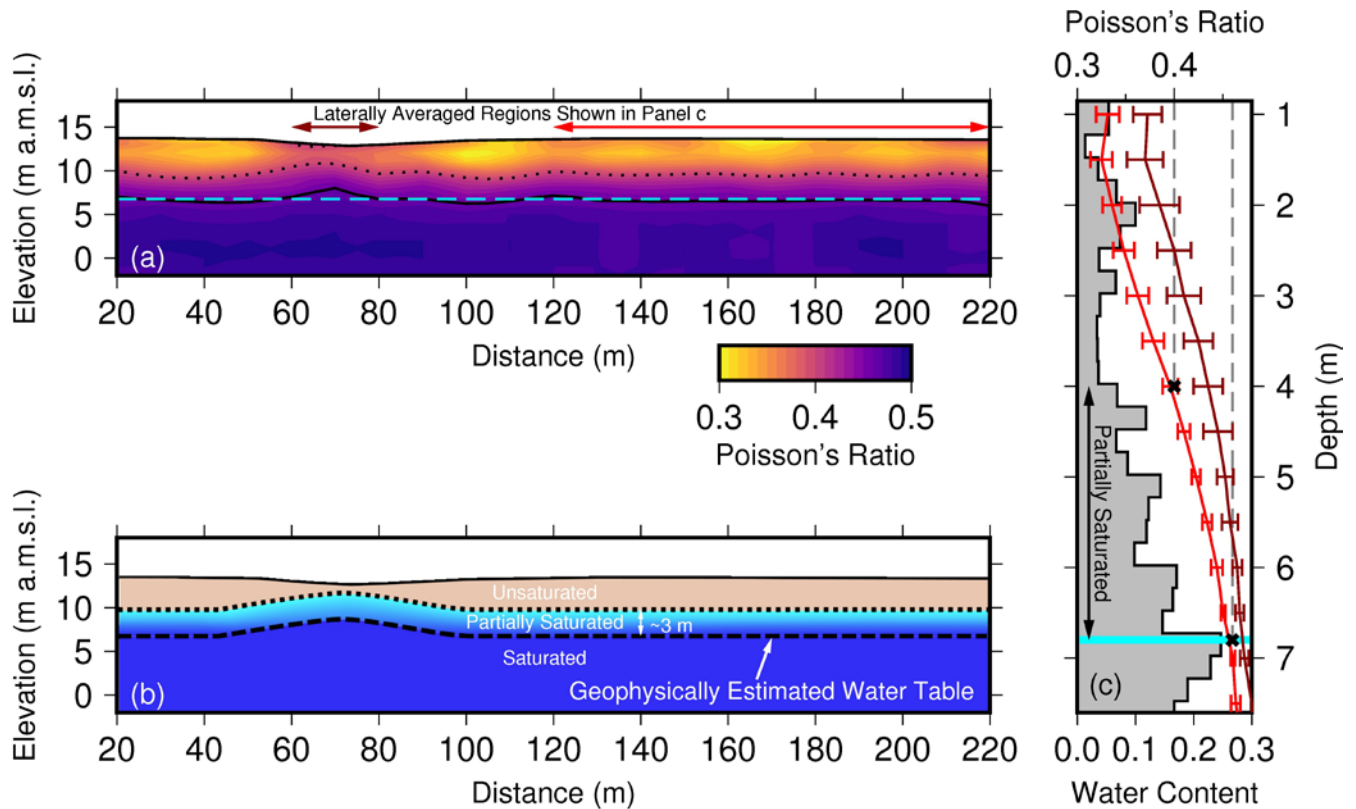
Figure 6 (a) Profile of Poisson's Ratio calculated using Equation 1 and the profiles shown Figures 2 and 3. The solid black contour represents a Poisson's ratio of 0.46. The dashed cyan line is the depth of water measured at the drill hole located at 220 m and assumed to be horizontal across the profile. The dotted contour line is the 0.4 contour line, which is consistent with a 3 m thick partially saturated region. (b) Geophysically interpreted hydrogeological cross-section. The unsaturated zone is quantified by areas with Poisson's ratios less than 0.40. The partially saturated region, with a thickness of approximately 3 m (determined from NMR in panel (c)) has Poisson's ratio between 0.4 and 0.46. The fully saturated region has Poisson's ratios greater than 0.46. The geophysically inferred water table is approximated by the 0.46 contour in panel (a). (c) The water content profile from Figure 5. The partially saturated region from 4 to 6.8 m depth is highlighted. The horizontal cyan bar is the manual water level measurement (6.8 m). Overlain on the water content profile are the two horizontally averaged 1D Poisson's ratio profiles. The red line is averaged from 120-220 m and the maroon line is averaged between 60 and 80 m along the profile. Black dashed lines and solid crosses highlight the Poisson's ratio contour values of 0.4 and 0.46 chosen in panel (a).
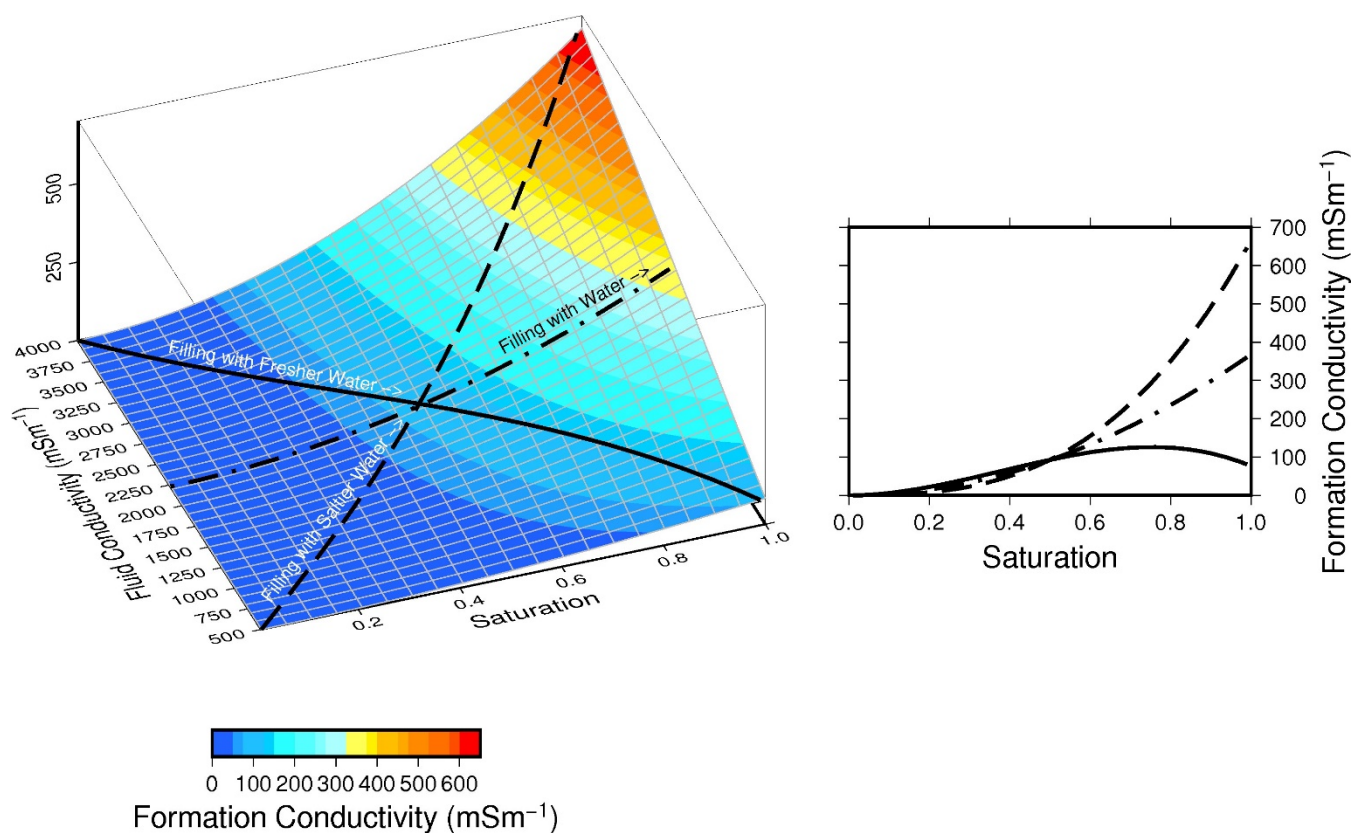
Figure 7. (a) The relationship between saturation, fluid conductivity, and formation conductivity calculated from Eq. 2, assuming a
constant porosity of 0.25, m=1.3, and n =2. The solid black line represents a case where the pore space is being filled with water that
gets less conductive (i.e. fresher). The dashed line is a case where water is being replaced with water that gets more conductive (i.e.
more saline). The dotted/dashed line is the case of filling the pores with water of the same conductivity. (b) The formation
conductivity as a function of saturation for the three end-member cases shown in panel a.

795
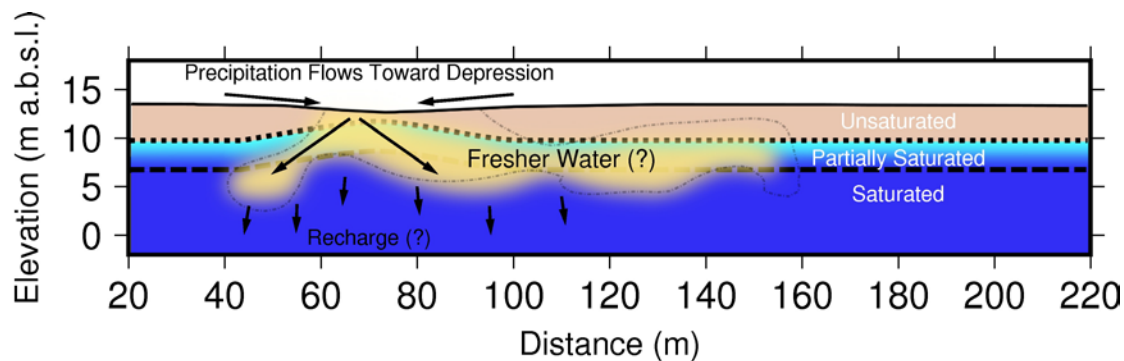
Figure 8. The final hydrogeological framework for the NAP. The underlying map is based on the seismic data (Figure 6b). The yellow region is our interpreted region of fresher water that has recharged the shallow unconfined aquifer system. Here water flows across the land surface and collects into the subtle ephemeral drainage feature. From there water is recharged into the underlying

800 **aquifer system and the hydraulic gradient drives recharging water away from the groundwater mound, to either side. During the recharge process, the fresher recharge water is mixing with the ambient saline groundwater of the shallow Quaternary aquifer.**